Eur J Nucl Med Mol Imaging
DOI 10.1007/s00259-013-2681-7

ORIGINAL ARTICLE

In vivo evaluation of a novel tau imaging tracer for Alzheimer's disease

Victor L. Villemagne · Shozo Furumoto · Michelle T. Fodero-Tavoletti · Rachel S. Mulligan · John Hodges · Ryuichi Harada · Paul Yates · Olivier Piguet · Svetlana Pejoska · Vincent Doré · Kazuhiko Yanai · Colin L. Masters · Yukitsuka Kudo · Christopher C. Rowe · Nobuyuki Okamura

Received: 14 October 2013 / Accepted: 20 December 2013

Abstract

Purpose Diagnosis of tauopathies such as Alzheimer's disease (AD) still relies on post-mortem examination of the human brain. A non-invasive method of determining brain tau burden in vivo would allow a better understanding of the pathophysiology of tauopathies. The purpose of the study was to evaluate ^{18}F-THK523 as a potential tau imaging tracer.

Methods Ten healthy elderly controls, three semantic dementia (SD) and ten AD patients underwent neuropsychological examination, MRI as well as ^{18}F-THK523 and ^{11}C-Pittsburgh compound B (PIB) positron emission tomography (PET) scans. Composite memory and non-memory scores, global and hippocampal brain volume, and partial volume-corrected tissue ratios for ^{18}F-THK523 and ^{11}C-PIB were estimated for all participants. Correlational analyses were performed between global and regional ^{18}F-THK523, ^{11}C-PIB, cognition and brain volumetrics.

Results ^{18}F-THK523 presented with fast reversible kinetics. Significantly higher ^{18}F-THK523 retention was observed in the temporal, parietal, orbitofrontal and hippocampi of AD patients when compared to healthy controls and SD patients. White matter retention was significantly higher than grey matter retention in all participants. The pattern of cortical ^{18}F-THK523 retention did not correlate with Aβ distribution as assessed by ^{11}C-PIB and followed the known distribution of tau in the AD brain, being higher in temporal and parietal areas than in the frontal region. Unlike ^{11}C-PIB, hippocampal ^{18}F-THK523 retention was correlated with several cognitive parameters and with hippocampal atrophy.

Conclusion ^{18}F-THK523 does not bind to Aβ in vivo, while following the known distribution of paired helical filaments (PHF)-tau in the brain. Significantly higher cortical ^{18}F-THK523 retention in AD patients as well as the association of hippocampal ^{18}F-THK523 retention with cognitive parameters and hippocampal volume suggests ^{18}F-THK523 selectively binds to tau in AD patients. Unfortunately, the very high ^{18}F-THK523 retention in white matter precludes simple visual inspection of the images, preventing its use in research or clinical settings.

Keywords Alzheimer's disease · Tau imaging · Aβ Imaging · Neurodegeneration · Brain

Electronic supplementary material The online version of this article (doi:10.1007/s00259-013-2681-7) contains supplementary material, which is available to authorized users.

V. L. Villemagne · M. T. Fodero-Tavoletti · R. S. Mulligan · P. Yates · S. Pejoska · V. Doré · C. C. Rowe
Centre for PET, Austin Health, Melbourne, Australia

V. L. Villemagne · M. T. Fodero-Tavoletti · C. L. Masters
The Mental Health Research Institute, Melbourne, Australia

S. Furumoto · R. Harada · K. Yanai · N. Okamura
Department of Pharmacology, Tohoku University School of Medicine, Sendai, Japan

J. Hodges · O. Piguet
Neuroscience Research Australia, Sydney, Australia

J. Hodges · O. Piguet
The University of New South Wales, Sydney, Australia

V. Doré
Preventative Health Flagship, CSIRO ICT, Brisbane, Australia

Y. Kudo
Innovation of New Biomedical Engineering Center, Tohoku University, Sendai, Japan

V. L. Villemagne (✉)
Department of Nuclear Medicine and Centre for PET, Austin Health, 145 Studley Rd, Heidelberg, VIC 3084, Australia
e-mail: villemagne@petnm.unimelb.edu.au

Published online: 11 February 2014

Introduction

Most neurodegenerative conditions are characterized by the aggregation of a misfolded protein such as Aβ and tau in Alzheimer's disease (AD), transactive response (TAR) DNA binding protein 43 kDa (TDP-43) in some forms of frontotemporal lobar degeneration (FTLD) such as semantic dementia (SD) or α-synuclein in Parkinson's disease. Tauopathies are neurodegenerative diseases characterized by the pathological accumulation of aggregated tau. AD is the most common tauopathy and the leading cause of dementia [1], but tau deposits are also found in other variants of FTLD, such as progressive non-fluent aphasia (PNFA) or in some cases of behavioural frontotemporal dementia (bFTD) [2]. Other tauopathies include Down's syndrome, Guam parkinsonism-dementia complex, frontotemporal dementia with parkinsonism linked to chromosome 17, corticobasal degeneration, progressive supranuclear palsy and chronic traumatic encephalopathy [3–5]. Definitive diagnosis of these neurodegenerative conditions can only be established after death. While these tauopathies share tau immunoreactivity in post-mortem brain examination, these tau aggregates can be composed of different tau isoforms displaying very distinct histopathological and ultrastructural differences [3, 6, 7]. In AD, these tau deposits can be recognized histologically as neurofibrillary tangles (NFTs) and neuropil threads as well as dystrophic neurites in senile plaques, whilst ultrastructurally they aggregate in paired helical filaments (PHF) [3, 4, 8]. While the underlying mechanisms leading to tau hyperphosphorylation, misfolding and aggregation remain unclear, tau aggregation and deposition follows a stereotypical and spatiotemporal pathway both at the intraneuronal level [8, 9] as well as in its topographical and neuroanatomical distribution in the brain [4, 10, 11].

The notion that tau dysregulation is a key mediator of neurodegeneration [12, 13] has stimulated the development of therapeutics for the treatment of AD and non-AD tauopathies [14–16]. Given these treatments are currently being developed, a non-invasive method of determining the tau burden in the brain would allow a better understanding of the pathophysiology of AD, FTLD and other tau-related neurodegenerative conditions. It will also lead to improvements in differential diagnostic accuracy and accelerate drug discovery by facilitating patient selection and monitor efficacy in novel anti-tau therapeutic trials. It would assist in the early and differential diagnosis of AD and non-AD tauopathies, while helping ascertain the relationship between the spatiotemporal distribution of tau aggregates in the brain to cognition and brain volumetrics. Development of tau imaging probes poses several more challenges than those associated with Aβ imaging, and these are mainly related to the idiosyncrasies of tau aggregation and deposition. In contrast to Aβ, most tau aggregates are intracellular, there are six tau isoforms and the different combinations of these isoforms manifest as different clinical phenotypes. Tau aggregates undergo a wide spectrum of post-translation modifications that, in addition to the combination of different isoforms, lead to diverse ultrastructural conformations and typical pathological lesions. Furthermore, tau aggregates coexist with other misfolded proteins sharing the same β-sheet secondary structure, as is in the case of AD where tau and Aβ are both co-localized in grey matter areas, where the concentrations of Aβ are, depending on the brain region, ~5–20 times higher than those of tau (for an in depth review see Villemagne et al. [17]).

In recent years, the main focus has been the development of selective ligands that allow early detection of Aβ deposition [18]. Among these tracers, ^{18}F-FDDNP was reported to non-selectively bind to both Aβ deposits and NFTs [19]. Phenylquinoline derivatives binding with high affinity and selectivity for tau aggregates have been developed as candidates for tau imaging agents at Tohoku University in Sendai, Japan [20]. Among them, ^{18}F-THK523 (THK523) was the first reported selective tau imaging tracer that can non-invasively detect tau deposits in a transgenic mouse brain [21]. This report was recently followed by several other potential tau tracer candidates [22–27].

After a careful in vitro evaluation, the initial in vivo characterization of a novel positron emission tomography (PET) neuroligand candidate requires to fulfill certain conditions such as safety at low tracer doses, possess high affinity and selectivity for the target, ability to cross the blood–brain barrier, display low non-specific binding with adequate regional distribution and its relation to parameters known to be associated with the intended target, suitable brain kinetics, lack of problematic radiolabelled metabolites [28] before it is applied to research or clinical use (Supplementary Fig. 1).

Therefore, the main objective of the present study was to characterize the in vivo suitability of THK523 for tau imaging in humans. The in vivo assessment comprised: (a) comparing the global and regional THK523 binding in healthy controls (HC), AD and SD patients, (b) assessing the relationship between THK523 retention and cognition, (c) assessing the relationship between THK523 retention and brain volumetrics and (d) comparing the regional brain distribution of THK523 with that of ^{11}C-Pittsburgh compound B (PIB) in the same participants.

Materials and methods

Participants

Written informed consent was obtained from all participants. Approval for the study was obtained from the Austin Health Human Research Ethics Committee. Elderly HC were recruited by advertisement in the community and dementia patients

were recruited from tertiary Memory Disorders Clinics or from physicians who sub-specialize in dementia care. All participants were classified on the basis of their clinical and neuropsychological performance by consensus of a neurologist and a neuropsychologist. Individuals classified as HC performed within normal limits on cognitive tests. AD patients met NINCDS-ADRDA criteria for probable AD [29], while three FTLD patients were classified as SD [30, 31]. None of the AD or FTLD patients had a family history of dementia.

Safety evaluation

Clinical, haematological and biochemical data on the safety of THK523 were collected for all participants. Heart rate, blood pressure, temperature and respiratory rate were measured immediately prior to injection and at 2, 15, 60 and 180 min post-injection. Immediately prior to THK523 injection, blood was drawn for routine haematology and biochemistry tests. An ECG was performed prior to injection of THK523 and at the completion of the scan, when they were also questioned for adverse events. All subjects were contacted by telephone 24 h later and questioned for adverse events. Between 5 and 8 days post-injection, subjects returned to be questioned for adverse events and for a physical examination, including a set of observations and repeat haematology and biochemistry testing.

Neuropsychological evaluation

In addition to the Mini-Mental State Examination (MMSE), Clinical Dementia Rating (CDR) and Clinical Dementia Rating Sum of Boxes (CDR SOB), the primary cognitive performance measures were composite episodic memory and non-memory scores generated as previously described [32]. Briefly, a composite episodic memory score was calculated by taking the average of the z scores (generated using 65 HC with both low PIB and normal MRI as the reference) for Rey Complex Figure Test (RCFT, 30 min) Long Delay and California Verbal Learning Test - Second Edition (CVLT-II) Long Delay and Logical Memory II. A composite non-memory score was calculated by taking the average of the z scores for the Boston Naming Test, letter fluency, category fluency, digit span forwards and backwards, digit symbol-coding and RCFT copy.

Image acquisition

Magnetic resonance imaging

Participants received an MRI on a 3 T Siemens TRIO MRI system (Siemens Healthcare, Erlangen, Germany) using the Alzheimer's Disease Neuroimaging Initiative (ADNI) 3D magnetization prepared rapid acquisition gradient echo (MPRAGE) sequence with 1×1 mm in-plane resolution and 1.2-mm slice thickness, repetition time (TR)/echo time (TE)/T1-weighted=2,300/2.98/900, flip angle 9° and field of view 240×256 and 160 slices. T2 -weighted fast spin-echo (FSE) and fluid-attenuated inversion recovery (FLAIR) sequences were also obtained. The interval between the THK523 and MRI studies was 1.6±3.3 months.

Positron emission tomography

Productions of ^{11}C-PIB and ^{18}F-THK523 were performed in the Centre for PET, Austin Hospital. ^{11}C-PIB was synthesized using the one-step ^{11}C-methyl triflate approach as previously described [18]. The decay-corrected average radiochemical yield for ^{11}C-PIB was 30 % with a radiochemical purity of >98 % and a specific activity of 30±7. 5 GBq/μmol. ^{18}F-THK523 was synthesized by nucleophilic substitution of the tosylate precursor [BF-241, 2-3 mg in 700 μl dimethyl sulphoxide (DMSO)]. The decay-corrected average radiochemical yield of the production of ^{18}F-THK523 was 22.5± 5 %, with a radiochemical purity of>95 % and a specific activity of 225.6±134.8 GBq/μmol (6.2±3.3 Ci/μmol).

A 30-min acquisition (6×5-min frames) on an Allegro™ PET camera started 40 min after injection of 300 MBq ^{11}C-PIB intravenously. A 90-min list-mode emission acquisition was performed in 3D mode after injection of 200 MBq ^{18}F-THK523. List-mode raw data were sorted offline into 6×30-s, 7×1-min, 4×2.5-min, 2×5-min and 6×10-min frames. The sorted sinograms were reconstructed using a 3D row action maximum likelihood algorithm (RAMLA). The interval between the THK523 and PIB PET studies was 0.3±3.8 months.

Tracer metabolism

Compound stability was assessed by incubating the tracer for 5, 30, 60, 90, 180 and 240 min with human S9 liver fractions.

Image analysis

Magnetic resonance imaging

Hippocampal and cortical grey matter volumes were obtained using a commercial fully automated volumetric measurement program (NeuroQuant®) applied to the 3D MPRAGE MRI images. The primary MRI performance measures were the grey cortical matter and hippocampal volumes normalized for total intracranial volume.

Positron emission tomography

PET images were processed using a semi-automatic region of interest (ROI) method as previously described [32]. Briefly,

THK523 and PIB PET images were co-registered to each individual's MRI using SPM8 (Wellcome Trust Centre for Neuroimaging, London, UK), and the same ROI template was applied. Given the reversible nature of THK523 kinetics, distribution volume ratios (DVR) were determined through graphical analysis of the dynamic data. Standardized uptake value ratios (SUVR) for PIB and THK523 as well as THK523 DVR were generated using the cerebellar cortex as reference region [18, 33]. Global tau and Aβ burden were expressed as the average SUVR for the following cortical ROIs: frontal (consisting of dorsolateral prefrontal, ventrolateral prefrontal and orbitofrontal regions), superior parietal, lateral temporal, lateral occipital and anterior and posterior cingulate for THK523 and PIB, respectively. As in previous studies, a PIB SUVR threshold of 1.5 was used to categorize high (PIB+) and low (PIB−) Aβ burden [32].

Partial volume correction (PVC), accounting for *both* grey matter atrophy and white matter spillover, was performed applying a three-compartment approach using PMOD 3.1 (PMOD Technologies Ltd., Zurich, Switzerland). DVR for THK523 were determined through graphical analysis of the last 45 min of the 90-min acquisition [33]. In order to avoid arterial blood sampling, a simplified approach was applied using the cerebellar cortex as reference region [18, 33]. Global DVR was calculated with the same regions used for the global SUVR. The primary outcome measure used for all THK523 and PIB assessments was the PVC SUVR.

Statistical evaluation

Normality of distribution was tested using the Shapiro-Wilk test and visual inspection of variable histograms. Statistical evaluations to establish differences between clinical groups means were performed using a Tukey-Kramer HSD test and by a Dunnett's test to compare each group with controls. Pearson's product-moment correlation analyses were conducted between imaging and clinical variables. Categorical differences were evaluated using Fisher's exact test. Effect size was measured with Cohen's *d*. All analyses were adjusted for age and corrected for multiple comparisons using false discovery rates. Data are presented as mean±standard deviation unless otherwise stated.

Results

Participants

Demographic characteristics of the participants are shown in Table 1. As expected, there were significant differences between the AD and SD patients and HC in cognitive performance and brain volumetrics. The AD group also presented with significantly higher PIB retention. While there were no significant differences between groups in age and gender, the AD group was less educated. While seven of the HC and the three SD patients showed low PIB retention, three of the HC presented with high PIB retention (Table 1).

No adverse events related to the study drug were observed or reported by participants or carers following the THK523 scan. There were no significant changes in clinical or biochemical parameters.

Tracer metabolism

THK523 was minimally metabolized, with 91, 81 and 65 % of unchanged parent compound remaining at 30, 90 and 180 min, respectively. No lipophilic radiometabolites were observed.

Brain kinetics

Brain THK523 radioactivity peaked between 3 and 6 min post-injection and the binding appeared to be reversible with rapid clearance from the brain (Fig. 1a, b). THK523 cleared fastest from cerebellar cortex and the clearance rate was the same for all groups (Fig. 1a, b). Clearance was slower from cortical areas in AD (Fig. 1b) than in HC (Fig. 1a) and SD patients. The ratio of cortical to cerebellar binding became constant in all participants by 50 min after injection (Fig. 1c).

Visual inspection

Visual inspection of the summed 60–90-min SUVR images revealed significantly higher THK523 retention in white matter than in grey matter regions, being significantly higher in AD patients than in HC or SD (Fig. 1d).

Assessment of tau burden

Regional analysis showed that there were no group differences in cerebellar cortex THK523 SUV, and there was no correlation between cerebellar cortex THK523 SUV with age in the whole cohort or with dementia severity in the AD group as assessed by MMSE (r=0.25, p=0.50), CDR (r=0.13, p=0.72) or CDR SOB (r=0.03, p=0.94).

While 60–90-min THK523 SUVR was estimated for all participants, four participants (two HC and two AD) were not able to complete the initial THK523 dynamic scan preventing calculation of DVR. In the remaining 16 subjects, significantly higher THK523 DVR were found in AD subjects in all cortical regions. The global THK523 DVR was 1.02±0.15 in AD vs 0.86±0.11 in HC (p=0.04, Cohen's effect size d=1.2). No significant differences were observed between HC and SD patients. Similar findings were observed with THK523

Table 1 Demographics

	HC (n=10)	SD (n=3)	AD (n=10)
Age	77.4±10.0	65.6±8.1	75.6±9.5
Gender (M/F)	3/7	1/2	4/6
MMSE	29.3±1.1	21.7±1.2*	16.7±6.6*
CDR	0.0	0.8±0.3*	1.3±0.6*
CDR SOB	0.1±0.2	2.5±1.1*	7.3±4.5*
Years of education	14.7±2.7	12.5±4.9	11.5±3.6*
Episodic memory scores	−0.4±0.6	−1.9±0.9*	−3.8±0.5*
Non-memory scores	−0.1±0.4	−1.4±1.2*	−3.4±1.6*
Hippocampal volume (cm^3)	5.1±0.6	4.3±0.3	4.1±1.0*
Aβ burden (PIB SUVR)	1.5±0.6 [PIB−=1.2±0.1 (n=7)] [PIB+=2.2±0.6 (n=3)]	1.1±0.1	2.9±0.5*

MMSE Mini-Mental State Examination, *CDR* Clinical Dementia Rating, *CDR SOB* Clinical Dementia Rating Sum of Boxes, *PIB* Pittsburgh compound B, *SUVR* standardized uptake value ratio, *PIB−* low PIB retention, *PIB+* high PIB retention

*Significantly different from HC (p<0.05)

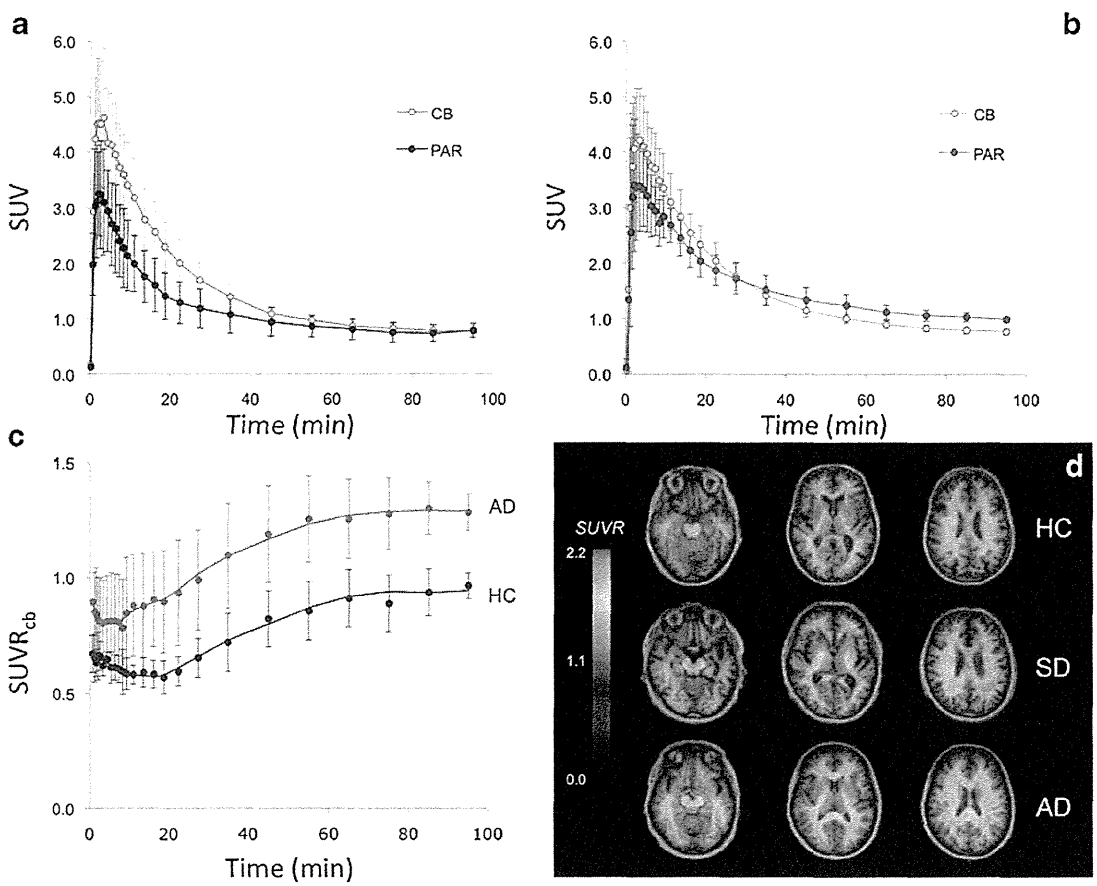

Fig. 1 ^{18}F-THK523 binding. Time-radioactivity curves for ^{18}F-THK523 in the parietal cortex (*PAR*) and the cerebellar grey matter (*CB*) in healthy controls (*HC*) (**a**) and Alzheimer's disease (*AD*) patients (**b**). There is fast ^{18}F-THK523 uptake in the brain followed by a fast clearance phase. While there is slower clearance with significantly higher retention in the parietal cortex of AD patients compared to HC, there are no significant differences in the cerebellar cortex uptake and clearance, further validating its use as reference region. **c** The total to non-specific binding ratios curves show significantly higher ^{18}F-THK523 retention in the parietal cortex of AD patients compared to HC. The specific binding reaches a plateau by 50 min post-injection. **d** Representative ^{18}F-THK523 PET images at three different brain levels in a 69-year-old female HC (MMSE 30, *top row*), a 73-year-old male semantic dementia (*SD*) patient (MMSE 21, *middle row*) and a 72-year-old female AD patient (MMSE 22, *bottom row*). Visual inspection of the images reveals no differences in ^{18}F-THK523 retention between HC and SD. There is higher white matter retention in AD compared to HC and SD. Data expressed as mean±SD of ten HC and ten AD patients

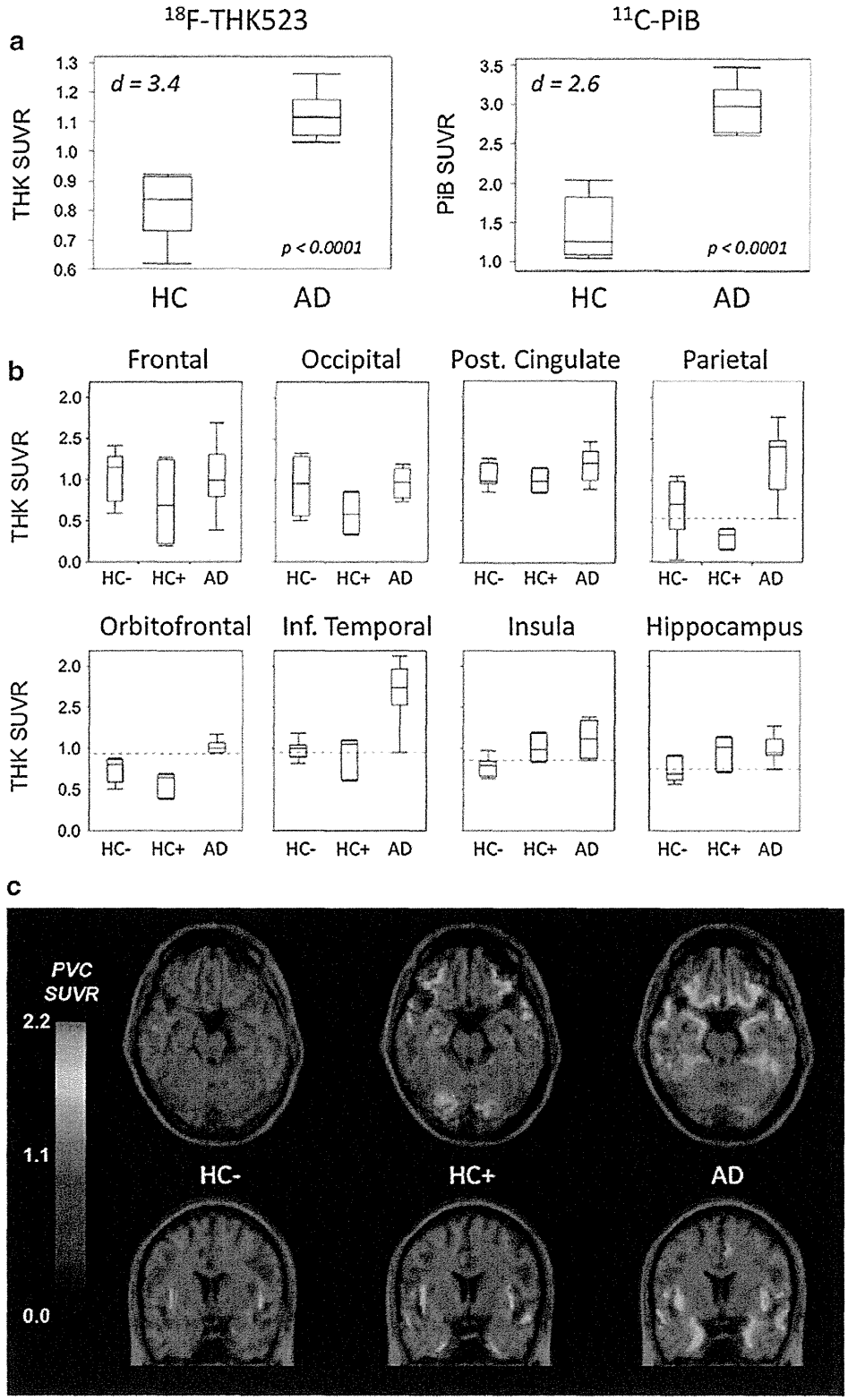

SUVR, and although SUVR values were higher than THK523 DVR, the rank order of the participants and the rank order of the regional values were identical, both showing the highest THK523 retention in temporal, parietal and hippocampus.

Table 2 Global and regional ^{18}F-THK523 and ^{11}C-PIB retention in AD

Region	THK SUVR				PIB SUVR			
	HC	AD	*p*	*d*	HC	AD	*p*	*d*
Frontal lobe	0.92±0.38	1.01±0.36	0.56	0.24	1.51±0.74	3.05±0.68	<0.0001	2.17
Orbitofrontal	0.68±0.16	1.06±0.24	<0.0001	1.87	1.42±0.50	2.91±0.58	<0.0001	2.74
Ant. cingulate	0.60±0.45	0.54±0.22	0.52	−0.19	1.61±0.75	2.98±0.59	<0.0001	2.04
Post. Cingulate	0.99±0.15	1.17±0.20	0.029	1.02	1.57±0.65	3.39±0.49	<0.0001	3.16
Parietal lobe	0.54±0.33	1.24±0.38	<0.0001	1.99	1.33±0.63	2.77±0.45	<0.0001	2.63
Lat. occipital lobe	0.81±0.33	0.91±0.29	0.38	0.31	1.35±0.35	2.32±0.38	<0.0001	2.66
Sup. temporal lobe	0.94±0.37	1.35±0.29	0.005	1.22	1.46±0.65	2.83±0.61	<0.0001	2.17
Inf. temporal lobe	0.96±0.16	1.81±0.58	<0.0001	2.00	1.52±0.62	2.89±0.51	<0.0001	2.42
Hippocampus	0.78±0.18	0.97±0.18	0.008	1.01	1.53±0.31	1.82±0.32	0.08	0.93
Insula	0.85±0.16	1.09±0.22	0.007	1.30	1.54±0.48	2.35±0.38	<0.0001	1.87
Striatum	0.39±0.16	0.46±0.25	0.65	0.33	1.79±0.76	2.98±0.64	0.0004	1.71
Subcortical white matter[a]	1.61±0.12	1.90±0.17	0.002	2.01	2.14±0.28	2.41±0.37	0.10	0.83
Neocortical	0.82±0.10	1.13±0.07	<0.0001	3.42	1.46±0.61	2.88±0.48	<0.0001	2.59

All images were partial volume corrected and then scaled and sampled. All results are adjusted for age
HC healthy control, *AD* Alzheimer's disease, *THK* ^{18}F-THK523, *PIB* ^{11}C-Pittsburgh compound B, *SUVR* standardized uptake value ratio, *d* Cohen's effect size *d*
[a] White matter SUVR are not partial volume corrected

THK523 SUVR correlated strongly with THK523 DVR in all cortical regions with a correlation coefficient of $r=0.85$ ($p<0.0001$) for the mean global measure.

Regional analysis of the non-partial volume-corrected images revealed significantly higher cortical THK523 retention in AD (Supplementary Fig. 2a) than in HC and SD patients. THK523 retention was also significantly higher in subcortical white matter in AD (Table 2). The spillover from the high retention in white matter was likely to contribute substantially to the radioactivity measured in grey matter; therefore, PVC of the images, correcting for *both* cortical grey matter atrophy and for white matter spillover, was performed. The PVC SUVR derived from the summed 60–90 min were subsequently used to assess THK523 retention as well as comparison with PIB and for correlation with brain volumetrics and cognitive parameters (Table 2). After PVC, while little or no THK523 retention was observed in cortical areas in HC, THK523 retention in AD patients was most prominent in cortical association areas, where only the temporal, parietal, hippocampal, orbitofrontal, and posterior cingulate regions (Supplementary Fig. 2b), brain areas known from post-mortem studies to contain substantial amounts of tau deposits in AD [10, 11], remained significant (Table 2). No significant differences were observed between HC and SD patients using either THK523 (Supplementary Table 1) or PIB (Supplementary Table 2). Global THK523 PVC SUVR in HC was 0.82±0.10 compared to 1.13±0.07 in AD ($p<0.0001$, Cohen's $d=3.4$) (Fig. 2).

◀ **Fig. 2** Global and regional retention of ^{18}F-THK523 and ^{11}C-PIB in AD. **a** Box plots for ^{18}F-THK523 (*left top panel*) and ^{11}C-PIB (*right top panel*) showing the global SUVR of both tracers. **b** When cognitively unimpaired HC with high (*HC+*) or low (*HC–*) ^{11}C-PIB retention were examined separately, it was observed that while ^{18}F-THK523 retention in isocortex of individuals with high ^{11}C-PIB retention aligned with those with low ^{11}C-PIB retention ^{18}F-THK523 retention in hippocampus and insula were not significantly different from the ^{18}F-THK523 retention in AD. *Red dotted lines* denote the bottom quartile of THK523 SUVR in AD patients. **c** Average parametric ^{18}F-THK523 transaxial and coronal partial volume-corrected (*PVC*) PET images overlaid on MRI of ten HC and ten AD patients, showing higher hippocampal and insular ^{18}F-THK523 retention on three HC with high (*HC+*) ^{11}C-PIB retention compared with seven HC with low (*HC–*) ^{11}C-PIB retention

Comparison of THK523 and PIB cortical retention

While seven of the ten HC and the three SD patients showed low Aβ burdens, all the AD patients and three HC presented with high Aβ burdens in the brain. In AD patients, the topographical pattern of cortical THK523 retention was clearly different from the cortical retention observed with PIB. While PIB was highest in the frontal, posterior cingulate, striatum and temporal cortices, THK523 was highest in temporal, parietal, hippocampus and posterior cingulate (Supplementary Fig. 3a). There was no correlation between the cortical THK523 SUVR and cortical PIB SUVR in the AD patients ($r=0.04$, $p=0.90$) (Supplementary Fig. 3b). Interestingly, in those HC with high Aβ burden (PIB+HC) while cortical THK523 retention was not significantly different to the cortical retention in PIB− HC, THK523 retention in the

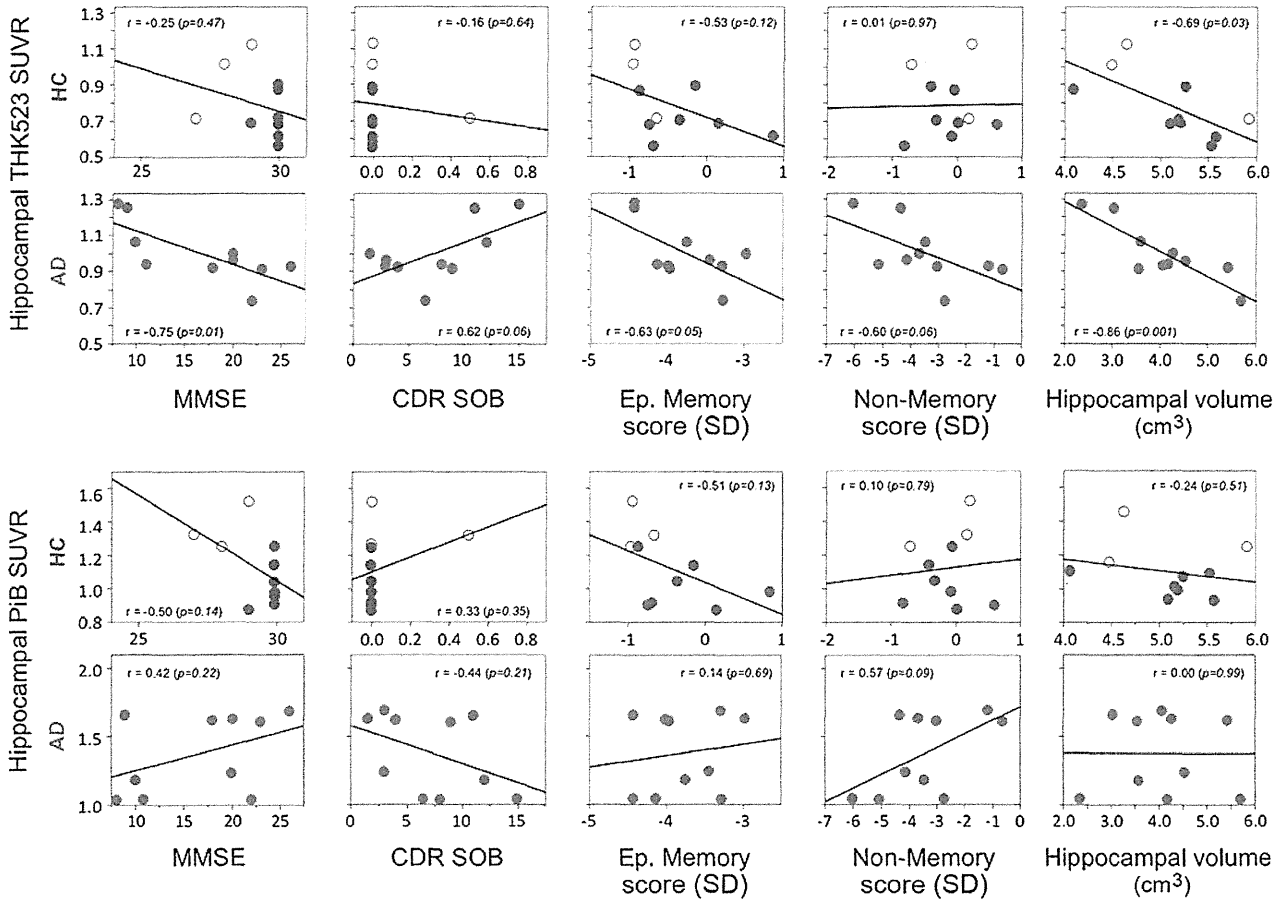

Fig. 3 Relationship between hippocampal ^{18}F-THK523 and ^{11}C-PIB retention with cognition and hippocampal volume. Regression analysis shows that while hippocampal ^{18}F-THK523 retention is not associated with cognition in HC, it is strongly associated with different cognitive parameters in AD patients (*top two rows*). On the other hand, hippocampal ^{18}F-THK523 retention is strongly associated with hippocampal volume in both HC and AD patients. There was no association between hippocampal ^{11}C-PIB retention (*bottom two rows*) with either cognitive parameters or hippocampal volume in any of the groups examined. All correlations were adjusted for age

hippocampus and insula was significantly higher than PIB− HC, but not significantly different from AD (Fig. 2).

Association between THK523 retention, cognition and brain volumetrics

While providing evidence of the general direction of the association between the different parameters (e.g. higher tau burden, lower cognitive performance), the associations derived from assessing all groups together tend to yield spurious correlations driven by the significant differences between the clinical groups. In order to avoid this issue, the associations with cognition and brain volumetrics were assessed in each clinical group separately.

In the case of THK523, there were no associations between cortical THK523 retention and cognitive parameters in HC, with the exception of the insula associated with episodic memory scores (r=−0.70, p=0.026). In the AD group, hippocampal THK523 retention was significantly associated with MMSE (r=−0.75, p=0.01) and episodic memory (r=−0.63, p=0.05) (Fig. 3). In the AD group, a strong trend was also observed between hippocampal THK523 retention, CDR SOB (r=0.62, p=0.055) and non-memory scores (r=−0.60, p=0.056). In regard to brain volumes, only hippocampal THK523 retention was significantly associated with hippocampal volume in both the HC (r=−0.69, p=0.03) and AD (r=−0.86, p=0.001) groups (Fig. 3). There were no correlations between global THK523 retention and cortical grey matter volume in any of the groups.

In the case of PIB, there were associations between PIB retention and MMSE in the orbitofrontal (r=−0.67, p=0.034), anterior (r=−0.65, p=0.04) and posterior cingulate (r=−0.78, p=0.007) regions of HC. In AD, there were some associations between PIB retention and cognitive parameters, but these correlations were, in every case, in the opposite direction as expected, where PIB retention in the anterior cingulate gyrus was positively associated with MMSE (r=0.63, p=0.049),

episodic memory (r=0.73, p=0.016) and non-memory scores (r=0.64, p=0.046) and inversely associated with CDR SOB (r=−0.68, p=0.03). There were no associations between hippocampal PIB retention and any cognitive parameter in any of the clinical groups (Fig. 3). There were no significant associations between global PIB retention and cortical grey matter volume in either HC or AD patients. In contrast to what was observed for hippocampal THK523 retention, there was no association between hippocampal PIB retention and hippocampal volume in any of the groups examined (Fig. 3).

Discussion

To the best of our knowledge, this is the first time a selective tau imaging agent has been thoroughly evaluated in human volunteers, assessing its associations with cognition and brain volumetrics, as well as a direct comparison with Aβ imaging using PIB.

Global cortical THK523 binding provided a very robust separation of AD patients from healthy elderly subjects (Cohen's d=3.4). Furthermore, cortical THK523 retention in AD patients followed the reported histopathological brain distribution of PHF-tau in AD [10, 11]. Examination of the brain kinetics of THK523 showed that it presents reversible binding kinetics, reaching apparent steady state about 50 min after injection of the radiotracer. Visual inspection of the THK523 images was hampered by the very high retention in white matter. In addition to the high non-specific binding, previous reports have demonstrated substantial concentrations of PHF-tau in white matter in AD [34, 35], suggesting THK523 retention in white matter might not solely reflect marked non-specific binding, but also some small degree of specific binding. Several factors were taken into account for the selection of the reference region. To date, no report has described tau deposition in the cerebellar cortex in sporadic AD [36]. There were no group differences in cerebellar cortex THK523 SUV, and there was no association between cerebellar cortex THK523 SUV with age in the whole cohort, or with dementia severity in the AD group, further supporting the use of the cerebellar cortex as reference region.

The regional brain distribution of THK523 showed a marked contrast when compared to that of PIB. While the highest PIB retention was observed in frontal, posterior cingulate, caudate and temporal cortices, the highest THK523 retention was observed in the inferior temporal, orbitofrontal, hippocampus, insula and parietal cortices. This was further confirmed by a lack of correlation between PIB SUVR and THK523 SUVR (r=0.04, p=0.90).

SD patients were included in the evaluation of THK523 as pathological controls [31]. Rather than tau aggregates, the vast majority of SD cases have been associated with the aggregation of TDP-43 [2, 31]. SD patients showed neither THK523 nor PIB retention in the brain (Supplementary Tables 1 and 2), suggesting the absence of both Aβ [37] and tau deposits in SD.

Three HC showed high cortical PIB retention (PIB+HC), consistent with previous PIB studies that have reported positive scans in 25–35 % of normal elderly individuals [38]. Despite the limited subsample size the finding is interesting because while cortical THK523 retention in PIB+HC was not significantly different from the cortical retention in PIB− HC, THK523 retention in the hippocampus and insula was significantly higher than in PIB− HC, but not significantly different from AD, suggesting that tau deposition in these regions might precede the dementia of AD [6, 39]. These findings might indicate that the combination of widespread cortical Aβ plus hippocampal tau deposition might not be enough to lead to significant cognitive impairment, requiring tau deposition in polymodal and unimodal association areas of the brain for objective cognitive impairment to be manifest [7, 10, 11].

As with Aβ imaging [40], longitudinal studies will assist in establishing the spatiotemporal patterns of tau deposition and help determine whether or not apparently healthy individuals with substantial hippocampal tau deposition will develop the AD phenotype, thus allowing very early, even preclinical diagnosis of AD, or if hippocampal tau deposits are just an age-associated process and only cortical tau deposition leads to cognitive impairment [39, 41].

In AD, hippocampal THK523 retention was associated with cognitive parameters. Similarly, hippocampal THK523 retention was associated with hippocampal volume in both HC and AD patients. Human post-mortem studies have shown that the density of NFTs strongly correlates with neurodegeneration and cognitive deficits, while Aβ plaque density does not [42, 43], a finding that was further confirmed through Aβ imaging studies [18, 32]. Furthermore, in stark contrast with Aβ plaques, NFTs are usually not present in associating cortical regions in cognitively unimpaired individuals [11, 18, 39].

As was previously reported in vitro [21, 44], several lines of evidence support the notion that THK523 selectively binds to PHF-tau and not to Aβ in vivo: (a) cortical THK523 retention is significantly higher in AD, following the known distribution of PHF-tau in the AD brain; (b) PIB and THK523 show different brain regional distribution patterns; (c) there is no correlation between PIB and THK523 retention; and (d) while hippocampal THK523 retention significantly correlates with cognitive parameters and hippocampal atrophy, hippocampal PIB retention does not.

While this was a first-in-human study, the limited sample size requires cautious interpretation of the findings. Furthermore, while our results suggest that ^{18}F-THK523 can reliably quantify PHF-tau deposition in vivo, there are serious limitations associated with the tracer itself. The high white matter THK523 retention, even if it might reflect some small degree of specific binding, precludes simple visual inspection of the

images and requires additional careful PVC even for a simple semi-quantitative analysis, preventing the use of THK523 in research or clinical settings.

Conclusion

This study has shown that despite selective, non-invasive in vivo assessment of PHF-tau in humans being possible, a single aspect of the in vivo behaviour of a tracer can derail its further development. This highlights the need for careful in vivo proof of concept studies at the initial stages of the development before embarking on more complex quantification approaches involving invasive procedures such as arterial cannulation or engaging in costly phase II studies. Better tau tracers, some of them already being evaluated in humans [23, 25–27], will be required for applications such as monitoring disease progression and assessing efficacy of anti-tau therapy. The development of ^{18}F-THK523 has shown to be a significant step towards the integration of tau imaging with Aβ imaging, moving us towards meeting the desired goal of earlier diagnosis of AD to assist the development of preventative treatments as well as identifying subjects for early therapeutic interventions.

Acknowledgements We thank Prof. Michael Woodward, Dr. John Merory, Dr. Gordon Chan, Dr. Kenneth Young, Dr. David Darby, Ms. Fiona Lamb and the Brain Research Institute for their assistance with this study. The study was partially supported by an Alzheimer Drug Discovery Foundation Research Grant (20101208 AFTD) and by a National Health and Medical Research Council of Australia Project Grant 1044361. The funding sources had no input into the design and conduct of the study; collection, management, analysis and interpretation of the data; and in the preparation, review, approval or decision to submit the manuscript for publication.

Conflicts of interest None.

References

1. Masters CL, Cappai R, Barnham KJ, Villemagne VL. Molecular mechanisms for Alzheimer's disease: implications for neuroimaging and therapeutics. J Neurochem 2006;97(6):1700–25. doi:10.1111/j.1471-4159.2006.03989.x.
2. Rabinovici GD, Miller BL. Frontotemporal lobar degeneration: epidemiology, pathophysiology, diagnosis and management. CNS Drugs 2010;24(5):375–98. doi:10.2165/11533100-000000000-00000.
3. Mohorko N, Bresjanac M. Tau protein and human tauopathies: an overview. Zdrav Vestn 2008;77(Suppl II):35–41.
4. Komori T. Tau-positive glial inclusions in progressive supranuclear palsy, corticobasal degeneration and Pick's disease. Brain Pathol 1999;9(4):663–79.
5. McKee AC, Cantu RC, Nowinski CJ, Hedley-Whyte ET, Gavett BE, Budson AE, et al. Chronic traumatic encephalopathy in athletes: progressive tauopathy after repetitive head injury. J Neuropathol Exp Neurol 2009;68(7):709–35. doi:10.1097/NEN.0b013e3181a9d503.
6. Delacourte A. Tauopathies: recent insights into old diseases. Folia Neuropathol 2005;43(4):244–57.
7. Buée L, Bussière T, Buée-Scherrer V, Delacourte A, Hof PR. Tau protein isoforms, phosphorylation and role in neurodegenerative disorders. Brain Res Brain Res Rev 2000;33(1):95–130.
8. Mandelkow E, von Bergen M, Biernat J, Mandelkow EM. Structural principles of tau and the paired helical filaments of Alzheimer's disease. Brain Pathol 2007;17(1):83–90. doi:10.1111/j.1750-3639.2007.00053.x.
9. Braak H, Braak E. Evolution of neuronal changes in the course of Alzheimer's disease. J Neural Transm Suppl 1998;53:127–40.
10. Braak H, Braak E. Staging of Alzheimer's disease-related neurofibrillary changes. Neurobiol Aging 1995;16(3):271–8. discussion 278–84.
11. Delacourte A, David JP, Sergeant N, Buée L, Wattez A, Vermersch P, et al. The biochemical pathway of neurofibrillary degeneration in aging and Alzheimer's disease. Neurology 1999;52(6):1158–65.
12. Goedert M, Jakes R. Mutations causing neurodegenerative tauopathies. Biochim Biophys Acta 2005;1739(2–3):240–50.
13. Roberson ED, Scearce-Levie K, Palop JJ, Yan F, Cheng IH, Wu T, et al. Reducing endogenous tau ameliorates amyloid beta-induced deficits in an Alzheimer's disease mouse model. Science 2007;316(5825):750–4.
14. Wischik CM, Edwards PC, Lai RY, Roth M, Harrington CR. Selective inhibition of Alzheimer disease-like tau aggregation by phenothiazines. Proc Natl Acad Sci U S A 1996;93(20):11213–8.
15. Brunden KR, Zhang B, Carroll J, Yao Y, Potuzak JS, Hogan AM, et al. Epothilone D improves microtubule density, axonal integrity, and cognition in a transgenic mouse model of tauopathy. J Neurosci 2010;30(41):13861–6. doi:10.1523/JNEUROSCI.3059-10.2010.
16. Bulic B, Pickhardt M, Mandelkow EM, Mandelkow E. Tau protein and tau aggregation inhibitors. Neuropharmacology 2010;59(4–5):276–89. doi:10.1016/j.neuropharm.2010.01.016.
17. Villemagne VL, Furumoto S, Fodero-Tavoletti MT, Harada R, Mulligan RS, Kudo T, et al. The challenges of tau imaging. Future Neurol 2012;7(4):409–21.
18. Rowe CC, Ng S, Ackermann U, Gong SJ, Pike K, Savage G, et al. Imaging beta-amyloid burden in aging and dementia. Neurology 2007;68(20):1718–25. doi:10.1212/01.wnl.0000261919.22630.ea.
19. Small GW, Kepe V, Ercoli LM, Siddarth P, Bookheimer SY, Miller KJ, et al. PET of brain amyloid and tau in mild cognitive impairment. N Engl J Med 2006;355(25):2652–63.
20. Okamura N, Suemoto T, Furumoto S, Suzuki M, Shimadzu H, Akatsu H, et al. Quinoline and benzimidazole derivatives: candidate probes for in vivo imaging of tau pathology in Alzheimer's disease. J Neurosci 2005;25(47):10857–62.
21. Fodero-Tavoletti MT, Okamura N, Furumoto S, Mulligan RS, Connor AR, McLean CA, et al. 18F-THK523: a novel in vivo tau imaging ligand for Alzheimer's disease. Brain 2011;134(Pt 4):1089–100. doi:10.1093/brain/awr038.
22. Zhang W, Arteaga J, Cashion DK, Chen G, Gangadharmath U, Gomez LF, et al. A highly selective and specific PET tracer for imaging of tau pathologies. J Alzheimers Dis 2012;31(3):601–12. doi:10.3233/JAD-2012-120712.
23. Chien DT, Bahri S, Szardenings AK, Walsh JC, Mu F, Su MY, et al. Early clinical PET imaging results with the novel PHF-tau radioligand [F-18]-T807. J Alzheimers Dis 2013;34(2):457–68. doi:10.3233/JAD-122059.
24. Shao XM, Carpenter GM, Desmond TJ, Sherman P, Quesada CA, Fawaz M, et al. Evaluation of [11C]N-methyl lansoprazole as a radiopharmaceutical for PET imaging of tau neurofibrillary tangles. ACS Med Chem Lett 2012;3(11):936–41.
25. Okamura N, Furumoto S, Harada R, Tago T, Yoshikawa T, Fodero-Tavoletti M, et al. Novel 18F-labeled arylquinoline derivatives for noninvasive imaging of tau pathology in Alzheimer disease. J Nucl Med 2013;54(8):1420–7. doi:10.2967/jnumed.112.117341.

26. Maruyama M, Shimada H, Suhara T, Shinotoh H, Ji B, Maeda J, et al. Imaging of tau pathology in a tauopathy mouse model and in Alzheimer patients compared to normal controls. Neuron 2013;79(6):1094–108. doi:10.1016/j.neuron.2013.07.037.
27. Chien DT, Szardenings AK, Bahri S, Walsh JC, Mu F, Xia C, et al. Early clinical PET imaging results with the novel PHF-tau radioligand [F18]-T808. J Alzheimers Dis 2014;38:171–84. doi:10.3233/JAD-130098.
28. Pike VW. PET radiotracers: crossing the blood–brain barrier and surviving metabolism. Trends Pharmacol Sci 2009;30(8):431–40. doi:10.1016/j.tips.2009.05.005.
29. McKhann G, Drachman D, Folstein M, Katzman R, Price D, Stadlan EM. Clinical diagnosis of Alzheimer's disease: report of the NINCDS-ADRDA Work Group under the auspices of Department of Health and Human Services Task Force on Alzheimer's Disease. Neurology 1984;34:939–44.
30. McKhann GM, Albert MS, Grossman M, Miller B, Dickson D, Trojanowski JQ, et al. Clinical and pathological diagnosis of frontotemporal dementia: report of the Work Group on Frontotemporal Dementia and Pick's Disease. Arch Neurol 2001;58(11):1803–9.
31. Hodges JR, Patterson K. Semantic dementia: a unique clinicopathological syndrome. Lancet Neurol 2007;6(11):1004–14.
32. Villemagne VL, Pike KE, Chételat G, Ellis KA, Mulligan RS, Bourgeat P, et al. Longitudinal assessment of Aβ and cognition in aging and Alzheimer disease. Ann Neurol 2011;69(1):181–92. doi:10.1002/ana.22248.
33. Price JC, Klunk WE, Lopresti BJ, Lu X, Hoge JA, Ziolko SK, et al. Kinetic modeling of amyloid binding in humans using PET imaging and Pittsburgh Compound-B. J Cereb Blood Flow Metab 2005;25(11):1528–47.
34. Mukaetova-Ladinska EB, Harrington CR, Roth M, Wischik CM. Biochemical and anatomical redistribution of tau protein in Alzheimer's disease. Am J Pathol 1993;143(2):565–78.
35. Khatoon S, Grundke-Iqbal I, Iqbal K. Levels of normal and abnormally phosphorylated tau in different cellular and regional compartments of Alzheimer disease and control brains. FEBS Lett 1994;351(1):80–4.
36. Larner AJ. The cerebellum in Alzheimer's disease. Dement Geriatr Cogn Disord 1997;8(4):203–9.
37. Rabinovici GD, Jagust WJ, Furst AJ, Ogar JM, Racine CA, Mormino EC, et al. Abeta amyloid and glucose metabolism in three variants of primary progressive aphasia. Ann Neurol 2008;64(4):388–401.
38. Rowe CC, Ellis KA, Rimajova M, Bourgeat P, Pike KE, Jones G, et al. Amyloid imaging results from the Australian Imaging, Biomarkers and Lifestyle (AIBL) study of aging. Neurobiol Aging 2010;31(8):1275–83. doi:10.1016/j.neurobiolaging.2010.04.007.
39. Delacourte A, Sergeant N, Wattez A, Maurage CA, Lebert F, Pasquier F, et al. Tau aggregation in the hippocampal formation: an ageing or a pathological process? Exp Gerontol 2002;37(10–11):1291–6.
40. Villemagne VL, Burnham S, Bourgeat P, Brown B, Ellis KA, Salvado O, et al. Amyloid beta deposition, neurodegeneration, and cognitive decline in sporadic Alzheimer's disease: a prospective cohort study. Lancet Neurol 2013;12(4):357–67. doi:10.1016/S1474-4422(13)70044-9.
41. Price JL, Morris JC. Tangles and plaques in nondemented aging and "preclinical" Alzheimer's disease. Ann Neurol 1999;45(3):358–68.
42. Arriagada PV, Growdon JH, Hedley-Whyte ET, Hyman BT. Neurofibrillary tangles but not senile plaques parallel duration and severity of Alzheimer's disease. Neurology 1992;42(3 Pt 1):631–9.
43. McLean CA, Cherny RA, Fraser FW, Fuller SJ, Smith MJ, Beyreuther K, et al. Soluble pool of Abeta amyloid as a determinant of severity of neurodegeneration in Alzheimer's disease. Ann Neurol 1999;46(6):860–6.
44. Harada R, Okamura N, Furumoto S, Tago T, Maruyama M, Higuchi M, et al. Comparison of the binding characteristics of [18F]THK-523 and other amyloid imaging tracers to Alzheimer's disease pathology. Eur J Nucl Med Mol Imaging 2013;40(1):125–32. doi:10.1007/s00259-012-2261-2.

Authors' contributions

Dr. Villemagne had full access to all the data in the study and takes responsibility for the integrity of the data and the accuracy of the data analysis

Drs. Villemagne, Furumoto, Fodero-Tavoletti, Kudo, Rowe and Okamura participated in the design, acquisition, analysis and interpretation of the data and writing of this manuscript.

Study concept and design: Villemagne, Okamura, Kudo, Rowe

Acquisition of data: Villemagne, Rowe, Fodero-Tavoletti, Pejoska, Yates, Piguet, Mulligan

Analysis and interpretation of data: Villemagne, Doré, Rowe, Okamura

Drafting of the manuscript: Villemagne, Okamura

Critical revision of the manuscript for important intellectual content: Villemagne, Furumoto, Rowe, Harada, Fodero-Tavoletti, Piguet, Hodges, Yanai, Masters, Kudo, Okamura

Statistical analysis: Villemagne, Okamura

Study supervision: Villemagne, Okamura

Shidahara et al. EJNMMI Research 2013, 3:32
http://www.ejnmmires.com/content/3/1/32

EJNMMI Research
a SpringerOpen Journal

ORIGINAL RESEARCH Open Access

Evaluation of the biodistribution and radiation dosimetry of the ^{18}F-labelled amyloid imaging probe [^{18}F]FACT in humans

Miho Shidahara[1,2*], Manabu Tashiro[2], Nobuyuki Okamura[3], Shozo Furumoto[3], Katsutoshi Furukawa[4], Shoichi Watanuki[2], Kotaro Hiraoka[2], Masayasu Miyake[2], Ren Iwata[5], Hajime Tamura[1], Hiroyuki Arai[4], Yukitsuka Kudo[6] and Kazuhiko Yanai[2,3]

Abstract

Background: The biodistribution and radiation dosimetry of the ^{18}F-labelled amyloid imaging probe ([^{18}F] FACT) was investigated in humans.

Methods: Six healthy subjects (three males and three females) were enrolled in this study. An average of 160.8 MBq of [^{18}F] FACT was intravenously administered, and then a series of whole-body PET scans were performed. Nineteen male and 20 female source organs, and the remainder of the body, were studied to estimate time-integrated activity coefficients. The mean absorbed dose in each target organ and the effective dose were estimated from the time-integrated activity coefficients in the source organs. Biodistribution data from [^{18}F] FACT in mice were also used to estimate absorbed doses and the effective dose in human subjects; this was compared with doses of [^{18}F] FACT estimated from human PET data.

Results: The highest mean absorbed doses estimated using human PET data were observed in the gallbladder (333 ± 251 μGy/MBq), liver (77.5 ± 14.5 μGy/MBq), small intestine (33.6 ± 30.7 μGy/MBq), upper large intestine (29.8 ± 15.0 μGy/MBq) and lower large intestine (25.2 ± 12.6 μGy/MBq). The average effective dose estimated from human PET data was 18.6 ± 3.74 μSv/MBq. The highest mean absorbed dose value estimated from the mouse data was observed in the small intestine (38.5 μGy/MBq), liver (25.5 μGy/MBq) and urinary bladder wall (43.1 μGy/MBq). The effective dose estimated from the mouse data was 14.8 μSv/MBq for [^{18}F] FACT.

Conclusions: The estimated effective dose from the human PET data indicated that the [^{18}F] FACT PET study was acceptable for clinical purposes.

Keywords: Positron emission tomography, Radiation dosimetry, Amyloid imaging, MIRD, [^{18}F] FACT

Background

Amyloid beta imaging

Deposits of amyloid β (Aβ) plaque are one of the pathological observations in patients with Alzheimer's disease (AD); Aβ deposition progresses at an earlier point than the current clinical diagnostic point for this disease [1]. For earlier diagnosis of AD and the evaluation of treatment efficacy, *in vivo* amyloid imaging using positron emission tomography (PET), which provides quantitation and visualisation of Aβ deposition in the brain, is useful. Therefore, several Aβ-binding probes dedicated for PET imaging have been developed [2,3].

Most of these PET Aβ ligands are ^{11}C-labelled compounds (physical half life ($T_{1/2}$), 20 min), and ^{18}F-labelled agents are being increasingly investigated owing to their long half life ($T_{1/2}$, 109.7 min). The long $T_{1/2}$ of ^{18}F enables several PET scans to be carried out from a single synthesis of labelled agent and also enables its commercial distribution to any PET facility. On the other hand, the longer the $T_{1/2}$ of the radioisotope gets, the greater is the radiation

* Correspondence: shidahara@med.tohoku.ac.jp
[1]Division of Medical Physics, Tohoku University School of Medicine, 2-1 Seiryo-machi, Aoba-ku, Sendai 980-8575, Japan
[2]Division of Cyclotron Nuclear Medicine, Cyclotron Radioisotope Center, Tohoku University, Sendai 980-8578, Japan
Full list of author information is available at the end of the article

dose exposure for the PET subject for the same administered dose of radioligand.

Importance of radiation dosimetry

For subjects undergoing PET, internal radiation exposure is inevitable, and the radiation dose delivered is proportional to the level of radioactivity of the injected radioligand and the number of injections. In the case of amyloid imaging, subjects often have multiple PET scans for diagnostic or therapeutic longitudinal monitoring of Aβ aggregation in the brain. Therefore, estimation of the radiation dose exposure from each PET radioligand and the use of well-balanced PET scan protocols taking into consideration subject risk and benefit are important.

Estimation of the internal radiation dose requires a time series measurement of the biodistribution of the injected radioligand. There are two ways to establish the biodistribution of a radioligand in humans: one is to extrapolate from data obtained in animal experiments [4] and the other is to use data from a clinical whole-body PET study [5]. Data extrapolated from animal experiments have been used to estimate clinical radiation dose. However, Sakata et al. reported that in some radioligands, there were considerable differences in organ dose or kinetics between human and animal experiments and that a whole-body PET study would be desirable for the initial clinical evaluation of new PET radioligands [6].

Previous biodistribution and dosimetry study for PET amyloid imaging

Recently, radiation dose exposures from several PET amyloid imaging agents have been reported using clinical whole-body PET scans. One of the popular amyloid ligands, Pittsburgh compound B ([^{11}C]PIB), has been extensively investigated with regard to its kinetics in the human body, and its effective radiation dose was found to be 4.74 μSv/MBq on average [7]. For ^{18}F-labelled PET amyloid radioligands, effective doses in humans have been reported as follows: ^{18}F-AV-45, 13 and 19.3 μSv/MBq [8,9]; ^{18}F-GE067, 33.8 μSv/MBq [10]; and ^{18}F-BAY94-9172, 14.7 μSv/MBq [11].

Aim of the present study

Fluorinated amyloid imaging compound ([^{18}F]FACT) is an ^{18}F-labelled amyloid imaging agent developed at Tohoku University [12]. Kudo and colleagues at this university have previously developed a ^{11}C amyloid imaging agent named [^{11}C]BF-227 [3]. [^{18}F]FACT is derived from [^{11}C]BF-227 by reducing its lipophilicity in order to reduce the nonspecific binding in the brain; AD patients showed significantly higher uptake of [^{18}F]FACT in the neocortex region relative to controls [12]. However, the biodistribution of [^{18}F]FACT in humans has not yet been investigated.

In the present study, the radiation dosimetry and biodistribution of [^{18}F]FACT was investigated in healthy elderly subjects who are the target group for PET amyloid imaging. In order to determine the discrepancy in the estimated radiation dose between human and animal experiments, biodistribution studies in mice involving [^{18}F]FACT were also conducted.

Methods

Subjects

PET studies were performed in three healthy male and in three healthy female volunteers (mean age ± standard deviation (SD), 76.3 ± 3.2 years). Subject characteristics are shown in Table 1. Both height and weight varied over a wide range (146 to 175 cm and 39 to 74 kg, respectively). All subjects were Japanese and were free of somatic and neuropsychiatric illness, as determined by clinical history and physical examination; one male subject (no. 1) had undergone a previous surgical operation involving gallbladder removal.

This study was approved by the Ethics Committee on Clinical Investigations of Tohoku University School of Medicine and was performed in accordance with the Declaration of Helsinki. Written informed consent was obtained from all subjects after a complete description of the study had been made.

Radiochemistry and radioligand purity

Figure 1 shows the chemical structure of ^{18}F-FACT. The radiochemical purity of the radioligand in the present clinical study ranged from 97.8% to 98.7% (mean ± SD, 98.33 ± 0.42%). The specific radioactivity ranged from 30.6 to 347.7 GBq/μmol at the time of injection (mean ± SD, 139.9 ± 116.2 GBq/μmol).

PET study

All whole-body PET studies were performed using a SET-2400W scanner (Shimadzu Inc., Kyoto, Japan) in two-dimensional (2D) mode [13]. The PET scanner acquired 63 image slices at a centre-to-centre interval of 3.125 mm and had a spatial resolution of 3.9 mm full width at half maximum (FWHM) and a *Z*-axis resolution of 6.5 mm FWHM at centre field of view [13].

An overview of scan protocols is shown in Figure 2. Four emission scans and two transmission scans (before administration and intermediate emission scans) using a ^{68}Ge/^{68}Ga source were performed, with the exception of subject no. 1 who had three emission scans. In the present series of PET studies and in other research projects, a 15-min PET brain scan using three-dimensional (3D) mode was performed after the first emission scan. At 2 min after intravenous administration of 142 to 180 MBq [^{18}F]FACT (mean ± SD, 160.8 ± 14.8 MBq; injection mass, 0.77 ± 0.66 ng), a series of whole-body PET

Table 1 Information regarding the human subjects

	Sex	Age (years)	Height (m)	Weight (kg)	BMI (kg/m^2)	History
Subject number						
1	M	77	1.59	61.2	24.2	Surgical removal of gallbladder
2	M	78	1.62	65	24.8	-
3	M	77	1.75	74	24.2	-
4	F	70	1.46	39	18.3	-
5	F	77	1.56	60.2	26.1	-
6	F	79	1.55	56	23.3	-
Mean ± 1 SD		76.3 ± 3.2	1.58 ± 0.75	59.2 ± 11.6	23.5 ± 2.7	

scans were performed. The schedule for the first and second transmission scans and the first, second, third and fourth emission scans was as follows: 6 positions × 4 min (24 min), 6 positions × 4 min (24 min), 6 positions × 3 min (18 min), 6 positions × 3 min (18 min), 6 positions × 3 min (18 min), and 6 positions × 4 min (24 min), respectively. The starting time of the second emission scan was different for each subject and was on average 55 min after the start of injection with a 5-min SD. The time gap between bed positions was 5 s. All emission data were reconstructed using OS-EM with iteration 16 and subset 2 after attenuation correction. Scatter correction was not performed because of the use of 2D mode data acquisition. The cross calibration factor of the scanner (Bq per ml/cps per voxel) was determined once per week using a cylindrical water phantom (25-cm length and 20-cm inner diameter) filled with ^{18}F solutions and by measuring the sample activity of the ^{18}F solutions at the well counter (BSS-3: Shimadzu Co., Ltd., Kyoto, Japan) [14].

Urination was controlled before, after and during the series of PET studies. In particular, during (15 min after the end of the first emission scan) and after the PET scans, subjects were asked to void. The volume and radioactivity levels of their urine samples were measured using a calibrated well counter.

MRI study

All subjects underwent T1-weighted magnetic resonance imaging (MRI) scans using a Signa 1.5-T machine (General Electric Inc., Milwaukee, WI, USA) within a week of the PET scans. For each position (brain, chest, abdomen and epigastric region), individual T1-weighted scans with a voxel size of 1.875 × 1.875 × 6.000 mm (TR = 460 ms, TE = 14 ms, image matrix = 256 × 256 × 40) were obtained with subjects holding their breath.

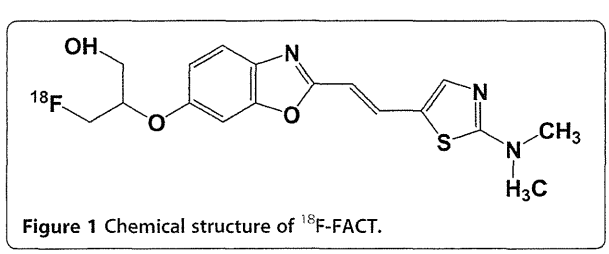

Figure 1 Chemical structure of ^{18}F-FACT.

Dosimetry

The Medical Internal Radiation Dose committee of the Society of Nuclear Medicine developed the algorithm to calculate absorbed dose D (the energy deposited per unit mass of medium (Gy)) in organs. The basic idea is that radiation energy from the radioisotope in the source organ is absorbed in the target organs, and the algorithm requires the net accumulated radioactivity in source organs as an input [15]. A PET scan contributes to quantitative knowledge on the whole-body distribution of radioisotope. In the present study, the accumulated activity in source organs was derived from PET measurements and the organ volumes of the reference male or female. The mean absorbed dose to the kth target organ is defined as follows:

$$\bar{D}(r_k) = \sum_h \tilde{A}_h \times S(r_k \leftarrow r_h) = \sum_h A_0 \times \tau_h \times S(r_k \leftarrow r_h),\ \tau_h = \frac{\tilde{A}_h}{A_0} \quad (1)$$

where $S(r_k \leftarrow r_h)$ is the absorbed dose in the kth target organ per unit of accumulated activity in the hth source organ, called the S value. $\tilde{A}_h$ is the number of disintegrations in the hth source organ, A_0 is the injected dose, and τ_h is the time-integrated activity coefficient in the hth source organ (equal to the number of disintegrations per unit activity administered). The effective dose E (Sv), as defined by the International Commission on Radiological Protection (ICRP) 60 [10], was obtained using the following equation:

$$E = \sum_i Q \times w_i \times D_i \quad (2)$$

where D_i is the absorbed dose of the ith target organ, w_i is the weighting risk factor in the ith target organ, and Q is the quality factor (Q = 1 for β- and γ-rays).

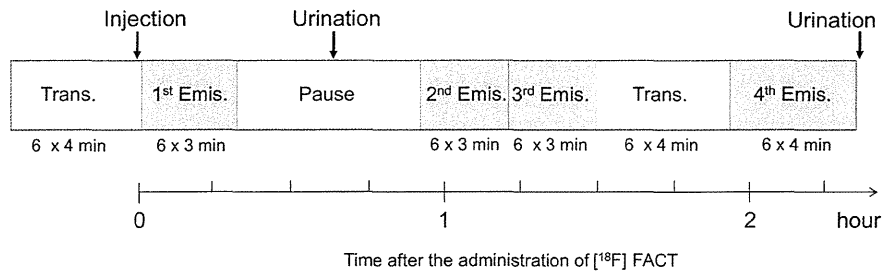

Figure 2 Overview of PET scan protocols. Four emission scans and two transmission scans (before and intermediate emission scans) with a $^{68}Ge/^{68}Ga$ source were performed. In particular, the second transmission scan was performed using a post-injection transmission scan.

Regions of interest

The number of source organs used for region-of-interest (ROI) drawing was 19 for male and 20 for female subjects. A detailed list of source organs is shown in Table 2. Two nuclear medicine physicians manually drew the ROIs using PMOD version 3.1 (PMOD Technologies, Zurich, Switzerland). All individual PET images and MRI images were co-registered to the first individual PET images using a rigid matching module of the same PMOD with a dissimilarity function of normalised mutual information (for MRI-to-PET cases) and the sum of the absolute difference (for PET-to-PET cases) algorithms.

For visceral organs with extremely high uptake (liver and gallbladder), individual ROIs were defined at a fixed

Table 2 [^{18}F]FACT time-integrated activity coefficients in the source organs

Organ	Human (MBq-h/MBq)							Mouse (MBq-h/MBq)
	Mean ± 1 SD	Subject 1	Subject 2	Subject 3	Subject 4	Subject 5	Subject 6	
Adrenal gland	5.38E−04 ± 2.98E−04	9.40E−04	8.40E−04	5.20E−04	3.70E−04	4.00E−04	1.60E−04	-
Brain	4.20E−02 ± 8.44E−03	5.41E−02	3.68E−02	3.53E−02	4.87E−02	4.42E−02	3.26E−02	6.99E−03
Breast	8.40E−03 ± 4.37E−03	1.14E−03	8.25E−03	5.59E−03	1.16E−02	1.19E−02	1.19E−02	-
Gallbladder content[a]	2.22E−01 ± 1.05E−01	-	1.49E−01	2.27E−01	3.88E−01	1.16E−01	2.31E−01	-
Lower large intestine content	2.12E−02 ± 2.03E−02	5.91E−02	1.06E−02	4.80E−03	2.27E−02	2.40E−02	5.96E−03	-
Small intestine content	8.78E−02 ± 1.08E−01	7.40E−02	3.74E−02	3.34E−02	3.06E−01	3.36E−02	4.25E−02	1.22E−01
Stomach content	6.71E−03 ± 2.28E−03	5.22E−03	6.23E−03	9.29E−03	9.84E−03	4.78E−03	4.87E−03	-
Upper large intestine content	2.55E−02 ± 1.89E−02	1.48E−02	4.88E−02	1.01E−02	4.99E−02	2.04E−02	8.85E−03	-
Heart content	1.12.E−02 ± 1.51E−03	1.24E−02	1.13E−02	1.02E−02	1.30E−02	1.15E−02	8.83E−03	3.95E−03
Heart wall	7.50E−03 ± 1.84E−03	4.63E−03	1.00E−02	8.84E−03	6.75E−03	7.28E−03	7.49E−03	2.39E−03
Kidney	1.34E−02 ± 3.27E−03	1.32E−02	1.16E−02	1.53E−02	1.89E−02	9.59E−03	1.20E−02	9.34E−03
Liver	4.92E−01 ± 1.05E−01	6.28E−01	5.85E−01	4.34E−01	5.15E−01	3.42E−01	4.49E−01	1.69E−01
Lung	3.55E−02 ± 1.16E−02	3.78E−02	5.31E−02	4.36E−02	2.46E−02	2.33E−02	3.08E−02	1.17E−02
Muscle	4.66E−01 ± 3.73E−01	9.43E−01	5.47E−01	7.97E−01	5.40E−02	4.12E−01	4.34E−02	1.57E−01
Ovary[b]	5.53E−04 ± 3.79E−05	-	-	-	5.70E−04	5.10E−04	5.80E−04	-
Pancreas	4.13E−03 ± 9.75E−04	6.10E−03	3.62E−03	3.93E−03	3.81E−03	3.55E−03	3.76E−03	-
Red marrow	3.98E−02 ± 4.33E−03	4.02E−02	3.83E−02	3.79E−02	4.59E−02	4.29E−02	3.34E−02	1.61E−02
Spleen	5.41E−03 ± 1.74E−03	8.64E−03	4.88E−03	3.83E−03	6.01E−03	4.77E−03	4.30E−03	1.28E−03
Testis[c]	5.77E−04 ± 4.67E−04	7.00E−04	6.10E−05	9.70E−04	-	-	-	-
Thyroid	3.53E−04 ± 1.55E−04	6.30E−04	3.70E−04	3.60E−04	2.40E−04	1.80E−04	3.40E−04	-
Urinary bladder contents	2.26E−02 ± 8.36E−03	1.70E−02	2.69E−02	1.55E−02	3.63E−02	2.49E−02	1.51E−02	6.56E−02
Uterus/uterine wall[b]	4.46E−03 ± 1.90E−03	-	-	-	6.42E−03	2.63E−03	4.33E−03	-
Remainder of the body	1.17 ± 3.63E−01	7.24E−01	1.06	9.48E−01	1.08	1.51	1.69	2.08

Averaged time-integrated activity coefficient (MBq-h/MBq) for the source organs (n = 6) from the whole-body PET data (n = 6) from experiments involving human subjects of [^{18}F]FACT and mice of [^{18}F]FACT. [a]Averaged value among five subjects excluding subject no. 1. [b]Average time-integrated activity coefficient among female subjects (n = 3). [c]Average time-integrated activity coefficient among male subjects (n = 3).

emission scan with about a 40% threshold against the maximum counts (first emission for the liver and third or fourth emission for the gallbladder). Then the ROI was applied to the other emission images with minor adjustment of its location or shape. For the intestines, if specific high uptake was observed, individual ROIs were defined on each time frame of the PET images with about a 10% threshold. If there was no specific high uptake in the intestines, and uptake could be regarded as uniform, individual ROIs were drawn around the corresponding area.

In order to obtain a typical radioactivity concentration within organs with less location mismatch between PET and the co-registered MRI images (brain, breast, heart wall, heart contents, kidney, liver, lung, muscle, bones, spleen and thyroid), individual ROIs were drawn on co-registered MRI images. For other low-uptake organs (adrenal gland, stomach contents, pancreas, ovary, uterus and testis), individual ROIs were drawn on each time frame of the PET images and referred to the co-registered MRI images. To avoid a partial volume effect, the size of the ROI for these MRI available organs was made slightly smaller than the entire source organ. It should also be noted that all activities in vertebrae ROIs was assumed to be in the red marrow in the present study.

Data analysis

Averaged time-activity curves for each organ were obtained using the ROI values from each subject's PET images. Because the PET images were decay-corrected at the start of each scan during the reconstruction procedure, the non-decay-corrected time-activity curves (C(t), Bq/ml) were re-calculated. During each whole-body emission scan, the bed position was moved from the foot to the head (six bed positions in total). However, we assumed that PET counts at all bed positions were acquired at the mid-scan time. Then, individual radioactivity concentration per injected dose A_0 (Bq) was extrapolated into the percent injected dose (%ID) of the reference subject as follows:

$$\%\mathrm{ID}(t)_{\mathrm{reference}} = \left(\frac{C(t)}{A_0}\right)_{\mathrm{individual}} \times V_{\mathrm{reference}} \qquad (3)$$

where V (ml) is the organ volume, and $V_{\mathrm{reference}}$ is V of the reference subject (we used a 70-kg adult male and 58-kg adult female as the male and female reference subjects) [16,17]. Even though some organs such as the intestine may change their volume over time, we used the reference subjects' organ volumes over the time period of the calculation of the %ID.

The time-integrated activity coefficient τ (Bq-h/Bq) in Equation 1 was obtained by fitting (%ID(t)) using a mono-exponential function and integrating from time zero to infinity. If the time-activity curve did not converge at the last PET scan (e.g. intestines and gallbladder), time-activity curves were fitted using two exponential functions, and then the area under the curve after the acquisition of the last image was calculated by assuming only physical decay of ^{18}F and no additional biologic clearance to be conservative [10]. The time-integrated activity coefficient for urinary bladder content was calculated by applying the dynamic urinary bladder model [10] to the urine samples with a bladder voiding interval of 2 h. The decay-corrected cumulative activity for urine was fitted using the equation $A \times (1 - \exp(-\ln(2) \times t / \tau))$, where τ is the biological decay and A is the fraction of activity released from the body. The sum of the time-integrated activity coefficient for the specific organs was subtracted from the time-integrated activity coefficient for the total body, which was calculated from the time integral of the decaying injected radioactivity. Then the residual of the subtraction was regarded as the time-integrated activity coefficient in the remainder of the body. All fitting procedures were undertaken using a mean fit of R^2 of 0.93 ± 0.13.

Finally, the time-integrated activity coefficient τ (Bq-h/Bq) was used to calculate the absorbed dose, D, in Equation 1 and the effective dose, E, in Equation 2. Both kinetics calculations (fitting and integration) and dose estimation were performed using OLINDA/EXM software version 1.0 (Department of Radiology and Radiological Sciences Vanderbilt University, Nashville, TN, USA) [17].

Animal experiments

The experimental protocols were reviewed by the Committee on the Ethics of Animal Experiments at Tohoku University School of Medicine and performed in accordance with the Guidelines for Animal Experiments issued by the Tohoku University School of Medicine. Estimated radiation dose of [^{18}F]FACT in the human subjects calculated from mouse data sets was compared with those of [^{18}F]FACT from human whole-body PET scans. An average dose of 1.4 MBq of [^{18}F]FACT was intravenously injected into ICR mice (age, 6 weeks; average body weight, 30 g) without anaesthesia. In the [^{18}F]FACT study, the mice were killed by cervical luxation at 2, 10, 30, 60 and 120 min ([^{18}F]FACT) after administration (n = 4 at each time point). The masses of the blood, heart, lung, liver, spleen, small intestine, kidney, brain and urine samples were measured, and activity was also measured using a well counter. Thigh bone and muscle were also sampled. The average uptake of the

radioligand into the male reference subject (70 kg) was extrapolated as follows [18]:

$$\%\mathrm{ID}(t)_{\mathrm{human}} = \left(\frac{\%\mathrm{ID}(t)}{\mathrm{mass}_{\mathrm{organ}}}\right)_{mouse} \times \left(\mathrm{mass}_{\mathrm{body}}\right)_{\mathrm{mouse}} \times \left(\frac{\mathrm{mass}_{\mathrm{organ}}}{\mathrm{mass}_{\mathrm{body}}}\right)_{human} \quad (4)$$

where the bodyweight of the mouse was assumed to be 30 for [^{18}F]FACT.

Finally, in the same manner as in the human PET data analysis, time-integrated activity coefficients, absorbed doses and effective doses were calculated using the OLINDA/EXM software version 1.0. Sampled blood, thighbone and urine were regarded as heart contents, red bone marrow and urinary bladder contents, respectively.

Results and discussion

Biodistribution of [^{18}F]FACT

Figure 3A is the coronal PET image for a single female subject (no. 5) and demonstrates the typical biodistribution of [^{18}F]FACT in the human body. The highest accumulations of this radioligand were observed in the gallbladder, liver, intestine and urinary bladder. For subject no. 1, [^{18}F]FACT contained in the bile was excreted from the liver to the duodenum through the biliary tract (Figure 3B). The biodistribution pattern of [^{18}F]FACT in human subjects showed a predominant hepatobiliary excretion, which is similar to what has been observed for other amyloid ligands, such as [^{11}C]PIB, [^{18}F]AV-45, [^{18}F]GE067 and [^{18}F]BAY94-9172 [7,8,10,11].

Figure 4 shows the decay-corrected time-activity curve of the %ID for typical source organs (brain, liver, spleen, lung, kidney, heart content, heart wall, muscle, red marrow, small intestine contents, gallbladder, upper large intestine contents and urinary bladder) from the six volunteers and the mice experiments. A significant difference between the %ID from humans and mice was observed in the brain, liver, spleen, heart contents, red marrow and urinary bladder, and these differences propagated the different results regarding dose estimation. In human subjects, ^{18}F uptake in the gallbladder contents and the intestines (Figure 4J,K,L) indicated larger individual variations in radioactivity uptake relative to other organs (e.g. the kidney as shown in Figure 4E). Radioactivity uptake in the upper large intestine showed propagation of both ligand kinetics and inter-subject variation from the gallbladder (Figure 4K,L). Scheinin et al. previously reported that inter-subject variation in ligand uptake ([^{11}C]PIB) in the gallbladder may be due to the quality and quantity of post-injection food intake [7]. In the present study, the subjects drank water during the interval between the first and second PET scans. This may have been responsible for the increase in inter-subject variation regarding the gallbladder. Furthermore, because the gallbladder uptake in some subjects had declined or remained at a low level at the final time points, we assumed that there was only physical radioactive decay after the last PET scans. However, this assumption may have led to a conservative estimation of the absorbed dose.

Figure 5 presents typical brain PET images obtained using [^{18}F]FACT at different time points with an

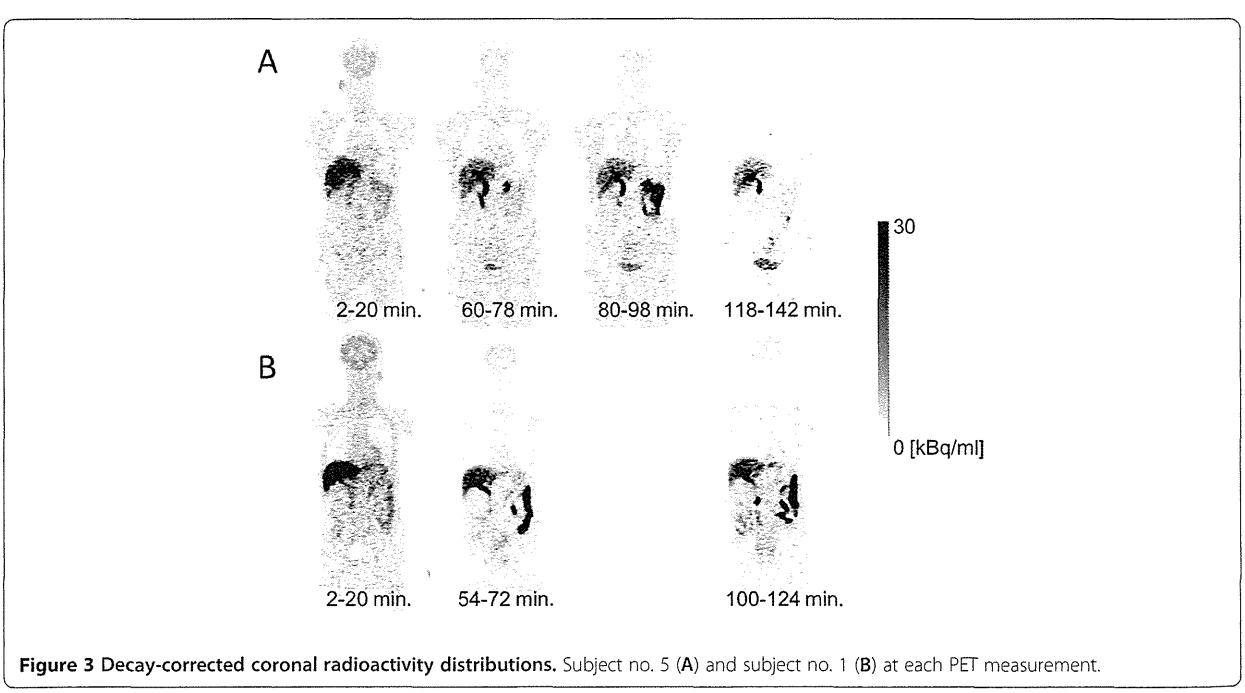

Figure 3 Decay-corrected coronal radioactivity distributions. Subject no. 5 (**A**) and subject no. 1 (**B**) at each PET measurement.

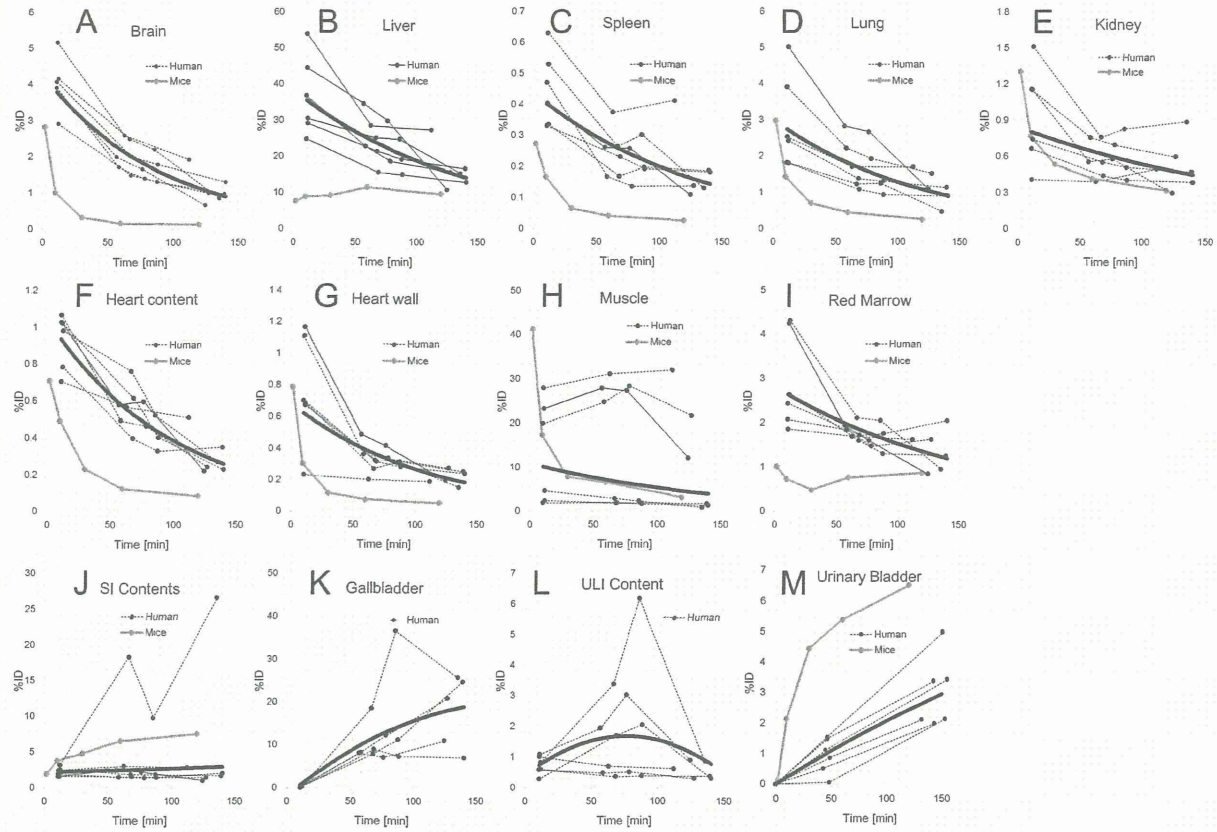

Figure 4 Decay-corrected time-activity curves of %ID. (**A**) Brain, (**B**) liver, (**C**) spleen, (**D**) lung, (**E**) kidney, (**F**) heart content, (**G**) heart wall, (**H**) muscle, (**I**) red marrow, (**J**) SI contents, (**K**) gallbladder, (**L**) ULI content and (**M**) urinary bladder for individual human (dashed black line) and averaged mice extrapolation (n = 4 at each time point, grey line). The solid black line indicates fitted curve using exponential function from all subjects' data points. The urinary bladder curve indicates accumulated activity excreted at all voiding/sampling moments.

acquisition time of 3 min (first, second and third emission) and 4 min (fourth emission). There was no significant retention of [^{18}F]FACT in the brain, and this may have been because the subject was normal.

Estimated dose of [^{18}F]FACT

The [^{18}F]FACT time-integrated activity coefficients in the source organs are shown in Table 2, and the absorbed doses are shown in Table 3. The averaged time-integrated activity coefficient for the gallbladder, as shown in Table 2, was calculated among five subjects excluding subject no. 1; however, in the case of the averaged absorbed and effective doses, subject no. 1 was included (Table 3).

High absorbed dose in humans was observed in the gallbladder (333 ± 251 μGy/MBq), liver (77.5 ± 14.5 μGy/MBq), small intestine (33.6 ± 30.7 μGy/MBq), upper large intestine (29.8 ± 15.0 μGy/MBq) and lower large intestine (25.2 ± 12.6 μGy/MBq). In mice, high absorbed doses were observed in the small intestine (38.5 μGy/MBq), liver (25.5 μGy/MBq) and urinary bladder wall (43.1 μGy/MBq) for [^{18}F]FACT (Table 3).

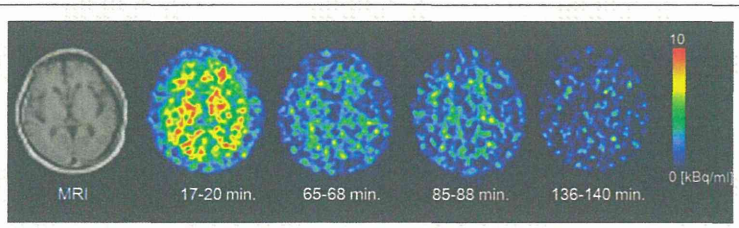

Figure 5 Decay-corrected brain PET images of subject no. 3 at different time points.

Table 3 Absorbed doses in the source organs

	Human			Mouse
	All subjects (n = 6)	Male (n = 3)	Female (n = 3)	
Organ				
Adrenal gland	1.96E01 ± 2.00	2.03E01	1.90E01	1.35E01
Brain	9.91 ± 1.82	8.95	1.09E01	4.17
Breasts	8.69 ± 2.55	6.68	1.07E01	9.90
Gallbladder wall	3.33E02 ± 2.51E02	2.16E02	4.50E02	1.68E01
Lower large intestine wall	2.52E01 ± 1.26E01	2.41E01	2.63E01	1.57E01
Small intestine	3.36E01 ± 3.07E01	2.07E01	4.64.E01	3.85E01
Stomach wall	1.61E01 ± 3.44	1.35E01	1.87E01	1.39E01
Upper large intestine wall	2.98E01 ± 1.50E01	2.36E01	3.59E01	1.83E01
Heart wall	1.62E01 ± 1.70	1.50E01	1.74E01	8.34
Kidneys	2.01E01 ± 4.30	1.85E01	2.17E01	1.32E01
Liver	7.75E01 ± 1.45E01	7.38E01	8.11E01	2.55E01
Lungs	1.46E01 ± 1.10	1.49E01	1.43E01	7.96
Muscle	1.03E01 ± 1.27	1.07E01	9.90	7.89
Ovary	1.67E01 ± 6.65	1.18E01	2.16E01	1.67E01
Pancreas	2.32E01 ± 3.11	2.17E01	2.47E01	1.45E01
Red marrow	1.31E01 ± 1.70	1.16E01	1.46E01	1.23E01
Osteogenic cells	1.60E01 ± 3.65	1.25E01	1.95E01	1.82E01
Skin	7.30 ± 1.39	5.99	8.60	8.70
Spleen	1.37E01 ± 2.48	1.27E01	1.48E01	7.83
Testis	7.32 ± 2.16	7.32	-	1.15E01
Thymus	1.00E01 ± 1.85	8.37	1.16E01	1.08E01
Thyroid	8.36 ± 1.38	8.86	7.86	1.10E01
Urinary bladder wall	2.23E01 ± 7.33	1.81E01	2.66E01	4.31E01
Uterus	1.67E01 ± 8.13	1.14E01	2.19E01	1.77E01
Total body	1.38E01 ± 1.63	1.22E01	1.53E01	1.22E01
Effective dose (μSv/MBq)	1.86E01 ± 3.74	1.64E01	2.09E01	1.48E01

Averaged absorbed dose estimates (μGy/MBq) for the target organs from the whole-body PET data (n = 6) from experiments involving human subjects of [^{18}F]FACT and mice of [^{18}F]FACT. Average absorbed dose for male subjects (n = 3).

The effective dose estimated from the human PET study was 18.6 ± 3.74 μSv/MBq. The effective doses of [^{18}F]FACT estimated from the clinical PET studies among other ^{18}F-labelled PET amyloid radioligands were as follows: [^{18}F]AV-45, 13 and 19.3 μSv/MBq [8,9]; [^{18}F]GE067, 33.8 μSv/MBq [10]; and [^{18}F]BAY94-9172, 14.67 μSv/MBq [11]. For PET analysis of [^{11}C]PIB, Scheinin et al. normalised the %ID using the ratio of individual and reference subjects' body weights (Equation 4) [7]. However, in the present study, we did not normalise the %ID data because there was a small difference between the effective dose with normalisation (17.6 ± 2.12 μSv/MBq) and the present effective dose (18.6 ± 3.74 μSv/MBq). Therefore, we concluded that body weight normalisation does not influence the effective dose.

The effective dose of [^{18}F]FACT from the mouse experiments (14.8 μSv/MBq) was underestimated as compared with that from the human subject PET studies (18.6 μSv/MBq) (Table 3). This discrepancy corresponded to 0.76 mSv (2.96 and 3.72 mSv from mice and humans, respectively) while assuming an injected activity of 200 MBq as a clinically relevant dose. The underestimation of absorbed dose in the mouse gallbladder (20 times lower) and liver (3 times lower) relative to the human PET studies may have been responsible for the underestimation of the effective dose. High absorbed doses in the liver, gallbladder and small intestine of mice indicated that the biodistribution pattern of [^{18}F]FACT in mice includes hepatobiliary excretion, as was observed in the PET scans involving human subjects. However,

the estimated absorbed dose in the gallbladder was 20 times lower than the estimate from human subject data sets because we could not remove the gallbladder of the mouse. Therefore, to evaluate the effective dose of [^{18}F]FACT in target organs, a whole-body PET scan of human subjects may be preferable as compared with the extrapolation from mouse experiments.

Clinical applicability of [^{18}F]FACT

The present whole-body PET study was performed using healthy elderly subjects and not patients with AD. Previously, Koole et al. speculated that if brain uptake of ^{18}F amyloid ligand increased by a factor of three, this will only influence estimation of the effective dose within 1%; however, when the subject had taken medication that changed the function of the hepatic metabolism, the estimated effective dose will vary with a larger range [10].

In the present series of PET studies, brain PET scans using the 3D mode were performed between the first and the second emission scan. Therefore, the injected dose for 2D whole-body scans was set to lower level than usual, and the averaged injected activity of 160.8 MBq corresponded to a radiation dose of 2.99 mSv per single administration. With regard to the optimal injected activity that can ensure sufficient image quality for clinical use, the peak noise-equivalent counts ratio (NECR) is often used in its determination. It has also been reported that the peak NECR in 2D mode was not reached with an acceptable range of injected activity, whereas in 3D mode, there was a distinct maximum for the NECR for which the corresponding injected activity was based on patient height and weight [19]. For the scanner used in our study, the NECR peak in 3D mode was reached at 4.44 kBq/ml using an 8,000-ml phantom [13]. When the subject's height and weight were assumed to be 170 cm and 60 kg, respectively, this assumption corresponded to the optimal injected dose of about 260 MBq. In a real situation, there exists the effect of the activity outside the axial FOV, and the optimal injected dose would be much lower. Injected activity indicates radiation dose; for example, 200 MBq indicates a radiation dose of 3.72 mSv. ICRP 62 [20] recommended that the maximum radiation dose that causes a 'minor to intermediate' increase of risk levels while preserving social benefit levels that are 'intermediate to moderate' has an effective limit of 10 mSv/year [20,21]. Thus, the maximum injectable activity is 537.6 MBq [^{18}F]FACT/year, and this injection dose limit allows two or three PET scans to be performed. Furthermore, amyloid imaging is mainly undertaken in elderly patients aged >50 years, even though for early detection of AD, patients aged <50 years will also have an amyloid PET scan. According to the guidance on medical exposures in medical and biomedical research by the European Commission [22], dose restrictions for patients aged over >50 years are not as strict as for younger patients. Therefore, considerably more multiple PET scans may be possible.

Conclusions

The effective dose of the ^{18}F-labelled amyloid imaging agent, [^{18}F]FACT, was found to be acceptable for clinical study.

Competing interests

The authors declare that they have no competing interests.

Authors' contributions

MS carried out the data analysis and interpretation and drafted the manuscript. TM, HT, YK and KY performed the study design and contributed to the intellectual discussion. NO, SF and RI performed the animal experiments and synthesis of PET probes. KF, SW, KH, MM and HA provided the clinical data. All authors read and approved the final manuscript.

Acknowledgements

We would like to thank Dr. Muneyuki Sakata from the Positron Medical Center, Tokyo Metropolitan Institute of Gerontology, and Dr. Hiroshi Watabe from the Cyclotron Radioisotope Center, Tohoku University, for their helpful advice regarding data analysis. This study was supported in part by Grants-in-Aid of Young Scientists (B) (no. 24700445) from the Ministry of Education, Culture, Sports, Science and Technology (MEXT), Japanese Government.

Author details

[1]Division of Medical Physics, Tohoku University School of Medicine, 2-1 Seiryo-machi, Aoba-ku, Sendai 980-8575, Japan. [2]Division of Cyclotron Nuclear Medicine, Cyclotron Radioisotope Center, Tohoku University, Sendai 980-8578, Japan. [3]Department of Pharmacology, Tohoku University School of Medicine, Sendai 980-8575, Japan. [4]Department of Geriatrics and Gerontology, Division of Brain Sciences, Institute of Development, Aging and Cancer, Tohoku University, Sendai 980-8575, Japan. [5]Division of Radiopharmaceutical Chemistry, Cyclotron Radioisotope Center, Tohoku University, Sendai 980-8578, Japan. [6]Clinical Research, Innovation and Education Center, Tohoku University Hospital, Sendai 980-8574, Japan.

Received: 23 January 2013 Accepted: 8 April 2013
Published: 24 April 2013

References

1. Hardy J, Selkoe DJ: **The amyloid hypothesis of Alzheimer's disease: progress and problems on the road to therapeutics.** *Science* 2002, 297:353–356.
2. Furumoto S, Okamura N, Iwata R, Yanai K, Arai H, Kudo Y: **Recent advances in the development of amyloid imaging agents.** *Curr Top Med Chem* 2007, 7:1773–1789.
3. Kudo Y, Okamura N, Furumoto S, Tashiro M, Furukawa K, Maruyama M, Itoh M, Iwata R, Yanai K, Arai H: **2-(2-[2-Dimethylaminothiazol-5-yl]ethenyl)-6-(2-[fluoro]ethoxy)benzoxazole: a novel PET agent for in vivo detection of dense amyloid plaques in Alzheimer's disease patients.** *J Nucl Med* 2007, 48:553–561.
4. Sakata M, Wu J, Toyohara J, Oda K, Ishikawa M, Ishii K, Hashimoto K, Ishiwata K: **Biodistribution and radiation dosimetry of the alpha7 nicotinic acetylcholine receptor ligand [^{11}C]CHIBA-1001 in humans.** *Nucl Med Biol* 2011, 38:443–448.
5. Deloar HM, Fujiwara T, Shidahara M, Nakamura T, Watabe H, Narita Y, Itoh M, Miyake M, Watanuki S: **Estimation of absorbed dose for 2-[F-18]fluoro-2-deoxy-D-glucose using whole-body positron emission tomography and magnetic resonance imaging.** *Eur J Nucl Med Mol Imaging* 1998, 25:565–574.
6. Sakata M, Oda K, Toyohara J, Ishii K, Nariai T, Ishiwata K: **Direct comparison of radiation dosimetry of six PET tracers using human whole-body imaging and murine biodistribution studies.** *Ann Nucl Med* 2013, 27:285–296.
7. Scheinin NM, Tolvanen TK, Wilson IA, Arponen EM, Nagren KA, Rinne JO: **Biodistribution and radiation dosimetry of the amyloid imaging agent ^{11}C-PIB in humans.** *J Nucl Med* 2007, 48:128–133.